

Revealing all states of dewetting of a thin gold layer on a silicon surface by nanosecond laser conditioning

Owen C. Ernst¹, David Uebel¹, Stefan Kayser², Felix Lange¹, Thomas Teubner¹,

Torsten Boeck¹

submitted: October 13, 2020

¹ Leibniz-Institut für Kristallzüchtung
Max-Born-Str. 2
12489 Berlin
Germany
E-Mail: owen.ernst@ikz-berlin.de
david.uebel@ikz-berlin.de
felix.lange@ikz-berlin.de
thomas.teubner@ikz-berlin.de
torsten.boeck@ikz-berlin.de

² Weierstrass Institute
Mohrenstr. 39
10117 Berlin
Germany
E-Mail: stefan.kayser@wias-berlin.de

No. 2777

Berlin 2020



Edited by
Weierstraß-Institut für Angewandte Analysis und Stochastik (WIAS)
Leibniz-Institut im Forschungsverbund Berlin e. V.
Mohrenstraße 39
10117 Berlin
Germany

Fax: +49 30 20372-303
E-Mail: preprint@wias-berlin.de
World Wide Web: <http://www.wias-berlin.de/>

Revealing all states of dewetting of a thin gold layer on a silicon surface by nanosecond laser conditioning

Owen C. Ernst, David Uebel, Stefan Kayser, Felix Lange, Thomas Teubner, Torsten Boeck

Abstract

Dewetting is a ubiquitous phenomenon which can be applied to the laser synthesis of nanoparticles. A classical spinodal dewetting process takes place in four successive states, which differ from each other in their morphology. In this study all states are revealed by interaction of pulsed nanosecond UV laser light with thin gold layers with thicknesses between 1 nm and 10 nm on (100) silicon wafers. The specific morphologies of the dewetting states are discussed with particular emphasis on the state boundaries. The main parameter determining which state is formed is not the duration for which the gold remains liquid, but rather the input energy provided by the laser. This shows that each state transition has a separate measurable activation energy. The temperature during the nanosecond pulses and the duration during which the gold remains liquid was determined by simulation using the COMSOL Multiphysics® software package. Using these calculations, an accurate local temperature profile and its development over time was simulated. An analytical study of the morphologies and formed structures was performed using Minkowski measures. With aid of this tool, the laser induced structures were compared with thermally annealed samples, with perfectly ordered structures and with perfectly random structures. The results show that both, structures of the laser induced and the annealed samples, strongly resemble the perfectly ordered structures. This reveals a close relationship between these structures and suggests that the phenomenon under investigation is indeed a spinodal dewetting generated by an internal material wave function.

The purposeful generation of these structures and the elucidation of the underlying mechanism of dewetting by ultrashort pulse lasers may assist the realisation of various technical elements such as nanowires in science and industry.

1. Introduction

Most material layer systems, being solid, liquid or gaseous, are metastable or even instable [1]. Consequently, the central question is not whether layers will collapse, but rather under what circumstances and how this will happen. In this work, a particular layer instability is to be examined more closely by nanosecond laser conditioning: Dewetting of thin metal layers towards nanoparticles respectively droplets. One or rather two decades ago, there were many attempts to describe the dewetting process of metals from a thermodynamic point of view [2][3]. Previously, it was rather observed how organic materials such as solvents or polymers dewet [4][5][6]. Considerations of the effective interface potential showed that two different mechanisms are possible: induced dewetting and spinodal dewetting[7]. Induced dewetting is the simpler case, where a layer gets disturbed or warped. A hole is formed in the layer by mechanical impact or a statistically random event. Dewetting starts from this hole. The material is piled up at the edge of the hole and pushed forward as the hole grows, forming droplets where holes meet [8]. The other mechanism is spinodal dewetting, where fluctuations in a layer's thickness lead to broad and simultaneous formation of holes and droplets. Spinodal dewetting can be divided into four states (Fig. 1): an initial layer state, a phase 1, a phase 2 and a final droplet state [7].

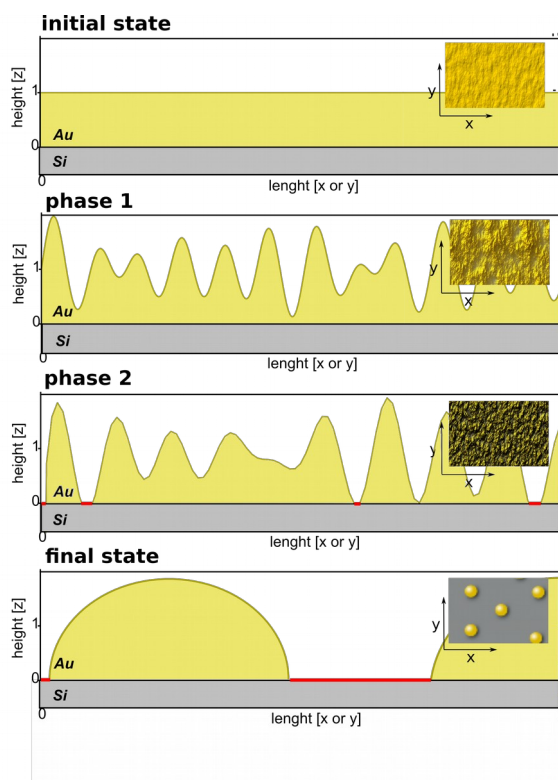


Figure 1. States of spinodal dewetting. Spinodal dewetting takes place in four different states. The initial state represents the as-grown gold layer. In phase 1 the layer starts to oscillate spatially. The oscillations reach the ground in phase 2. This is represented by the red areas. The red, dry areas expand till droplets are formed in the final state.

The initial layer state represents a homogeneous, undisturbed layer. In phase 1 the layer experiences heat and consequentially increased Brownian motion. The effective interfacial potential can possibly intensify this movement and create a spatial oscillation or warping in the layer thickness. These spatial oscillations are stable in phase 1, but become unstable in phase 2. Here, the motion gets amplified even more, which leads to valleys of the material waves hitting the underlying substrate. In this way a hole is formed in the layer and this hole grows in the same way as they grow in the induced mechanism. The main difference is that in spinodal dewetting, the holes are not created randomly, but in the order dictated by heat-induced warping amplified by the effective interface potential.

First, these states of dewetting were not identified individually, but successfully isolated from each other, whereby the correctness of the postulates and energy calculations could be proven [9][10][11]. This was done by thermally induced dewetting [12] and also by experiments in which heat was applied to the thin metal layers by a laser [13][14][15]. In this work, these earlier results will be not only confirmed. The focus lies predominantly on the transitions between the different states of dewetting. For this purpose, a precise adjustment of the laser parameters and a detailed description of the heat influence of the laser in the gold-silicon system were carried out. The COMSOL Multiphysics® software package provides a detailed model of the dynamic temperatures and heat flows in the system [16]. Numerical simulations such as these provide a reproducible method for solving complex systems [17]. This allows new and more specific insights into the system than it was previously possible with classical analytical calculations, which was done in great detail by other scientists for heat flows in laser-induced dewetting [18].

Additionally, Minkowski measures were computed to estimate the quality of the transition states of the laser-treated layers compared to the thermally treated ones. Minkowski functionals are an effective tool to compare structures with each other and to find relations between structures which are not visible to the eye. The Minkowski functionalism offers a statistically stable method of integral geometry analysis, in which integration is performed over the entirety of all boundaries of a structure in all domains [19]. It is remarkable that the topology and geometry can be investigated in great detail for very diverse structures and morphologies [20]. This makes them suitable both for large-scale systems whose size is unknown or of which only a very small part can be observed, and for micro- and nanoscopic systems that are difficult to study, image or reproduce. For this reason, Minkowski functionalism is a highly valued tool in theoretical and statistical physics to describe a

variety of widely different systems, such as galaxies in astronomy [21][22][23], chemical reactions in physical chemistry [24][25][26] or, as also demonstrated here, the motion of ensembles of atoms to gain a deeper insight into dewetting mechanisms [27]. In this work, Minkowski measures are used to determine whether the dewetting process is random or whether there is an internal ordering mechanism. By determining whether the structures created by dewetting are randomly arranged or ordered, it is possible to distinguish between induced dewetting and spinodal dewetting.

For this study, a thin gold layer in the thickness range of 1 nm to 10 nm on a (100) silicon wafer is treated with a 266 nm nanosecond laser. The system of gold on silicon was chosen for two reasons: Firstly, early qualitative descriptions were made for this system, which promotes a quantitative experiment [28]. And secondly, gold on silicon is a promising material system for many applications - especially in the form of gold droplets on silicon [29][30]. For example, gold nanodroplets can be used as nanocatalysts for semiconductor nanowires [31][32]. Vaporised material such as silicon or germanium dissolves into the gold droplet by the vapour-liquid-solid process. During this solvation process the droplet becomes supersaturated and excess material precipitates at its bottom. As a result, a nanowire grows. These 1-D nanostructures are not only of scientific value, but are also promising for various technical applications such as thermoelectrics [33][34][35], low-power field-effect transistors [36] or other gate-allround architectures[37]. In this case, dewetting can be used to actively create structures for further processing. However, there exist other examples where dewetting damages electrical appliances when contact or protective layers become unstable and deteriorate [38][39]. Both the preparation of these desired structures and the avoidance of unwanted instabilities are crucial for industrial processes. However, this requires thorough knowledge of all relevant processes. For this reason, the transition of all dewetting states and their morphological and energetic behaviour have been investigated closely in this work.

2. Material and methods

2.1 Preparation of substrates

(100) oriented 3 inch Si wafers with an initial surface roughness (RMS) of 0.1 nm were used. To dissolve the native silicon oxide and to passivate the free surface bonds by hydrogen, the substrates were immersed for 10 s in 2 % HF solution and rinsed in deionized water.

Au deposition was carried out in a molecular beam epitaxy (MBE) chamber at a base pressure of 2×10^{-10} mbar. To reduce the amount of water inside the MBE chamber, the substrate was annealed

at 870 K for 1 h in a separate preparation chamber. Before Au deposition, the substrates were annealed at 1170 K for 5 min to guarantee an oxide-free and reconstructed 2×1 Si(100) surface.

Then, 1 nm Au was evaporated from an effusion cell onto the substrate with a nominal deposition rate of 0.01 nm s^{-1} at room temperature. The absence of characteristic RHEED reflections after the deposition process indicates an amorphous Au layer on the crystalline substrate.

2.2 Laser conditioning

For the laser-treatment of the Si/Au samples, a Q-state solid state laser (FQSS-266-200, CryLas GmbH) with a wavelength of 266 nm was used. It provides pulses with an energy of $190 \mu\text{J}$ with pulse widths of 1.4 ns (FWHM – space of time) with a repetition rate of 170 μs . Samples with different gold thicknesses from 1 nm to 10 nm were repeatedly treated with the laser: 1'000 pulses, 10'000 pulses, and 100'000 pulses were applied to samples of each thickness. The laser system is positioned underneath a vacuum chamber with a fused quartz window which is transparent to UV light. To position laser spots on the sample surface, a beam-shaping optic consisting of an adjustable neutral density filter wheel, several mirrors and an iris aperture is used. A programmable laser scan head (SCANcube, SCANLAB GmbH) is used to precisely limit the time and thus the number of pulses that the sample is exposed to the laser. The energy distribution of the laser was measured in the sample position before the experiments with a beam profiler (CinCam CMOS-1202, CINOGY Technologies GmbH). The energy of one laser pulse was repeatedly measured without the sample between the experiments. The detector is positioned behind the sample plane outside the vacuum chamber and therefore behind another UV-transparent fused quartz glass window. During lasing the chamber is held at a vacuum of $5 \cdot 10^{-6}$ mbar. Fig. 2 shows a sketch of the used laser system.

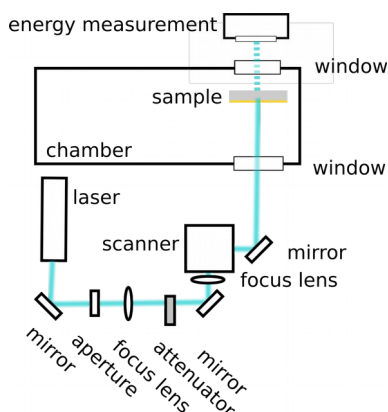


Figure 2. Sketch of the used laser system. A 266 nm nanosecond-laser is used to treat a thin gold layer on a silicon sample. Since gold is almost transparent for UV light, the laser beam is absorbed only by silicon.

2.3 Thermal treatment

A couple of samples were annealed at 800 K or 1400 K for 10 min by a wafer heater in a high vacuum chamber (10^{-6} mbar) as reference to the laser experiments.

2.4 Modelling

2.4.1 Implementation of COMSOL simulation

The heat transfer in the silicon-gold system was modelled with the heat transfer module of the COMSOL Multiphysics® 5.4 software package in 2.5 dimensions using a finite element approach (FEM) and MUMPS solver [17].

The model as used for COMSOL calculations is composed of a cylindrical stack of a 200 nm thick silicon wafer, of an infinitesimal small interface between silicon and gold, and of a 5 nm thick gold layer (Fig. 3a).

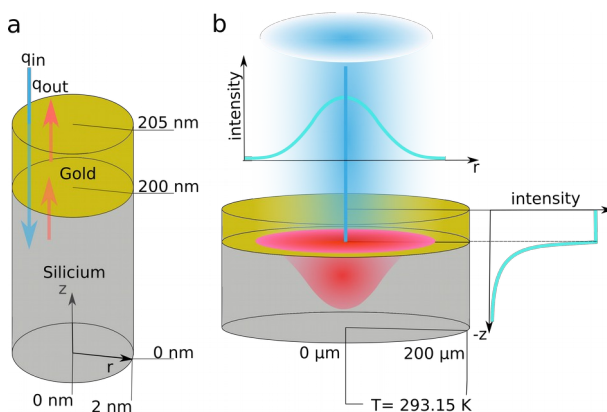


Figure 3. Sketch of material model used in the COMSOL Multiphysics® simulation. (a) The simulation is based on a cylindrical stack of silicon and gold with separately treated interface in between. Energy, respectively heat \mathbf{q}_{in} and \mathbf{q}_{out} , can enter and leave the system through the boundaries in z -direction. (b) The input-energy serves a 266 nm laser pulse with Gaussian shape in time and space. The energy is absorbed inside the silicon taking into account Beer-Lambert-Bouguer law. The backside is set to constant room temperature. The whole system will cool down to this temperature in less than 170 μs .

The radius of each cylindrical stack is diminutive compared to the assumed laser pulse. Due to its modest size, it is assumed that no heat leaves the cylindrical stack through the side walls. Fig. 3b pictures a larger cylinder representing the entire laser pulse function. Due to the low thickness of the thin gold layers, it is assumed no heat is generated within the gold layer. The assumption heat originates exclusively in silicon is underlined by the fact that the absorption of UV light in gold generates ballistic electrons [40][41]. These electrons are most likely to be diverted into the silicon, where they lead to additional heating [42]. The heat flows back through the boundary layer into the gold film and heat it up indirectly. Fig. 3b shows the intensity of the generated heat considering the penetration depth of the laser according to the Beer-Lambert-Bouguer law. The backside of the

silicon cylinder is held at a constant temperature of 293.15 K. Measurements indicate a Gaussian shape for the laser pulses in time and space. This results in an energy profile in the silicon that can be described as

$$f_{(z,r,t)} = \sqrt[3]{\frac{1}{d_p} e^{\frac{200-z}{d_p}} \cdot \frac{1}{2\pi \cdot \sigma_L^2} e^{\frac{-(r-r_0)^2}{2 \cdot \sigma_L^2}} \cdot \frac{E_0}{\sqrt{2\pi \cdot \sigma_t}} e^{\frac{-(t-t_0)^2}{2 \cdot \sigma_t^2}}} \text{ [J]}, \quad (1)$$

With $d_p = 7.3 \times 10^{-9} \text{ m}$, $\sigma_L = 4.7 \times 10^{-5} \text{ m}$, $E_0 = 7.5 \times 10^{-19} \text{ J}$ and $\sigma_t = 6.1 \times 10^{-10} \text{ s}$.

Accordingly, the laser pulse has a lateral extension of 100 μm and lasts 1.4 ns (FWHM in each case).

To calculate the change in temperature over time, the heat equation was used

$$\frac{\partial T}{\partial t} = \frac{\kappa \nabla^2 T + q}{\rho C_p}.$$

A detailed derivation of this formula can be found in [16].

Table 1 contains all important material parameters used in the simulation.

Table 1. Values and formulars for material paramters used in the simulation.

Density [kg m ⁻³]	gold _{solid} [43]	$1.93 \cdot 10^4 - 1.99 (T - 300)$
	gold _{liquid} [44]	$1.74 \cdot 10^4 - 1.44 (T - 1300)$
	silicon _{solid} [45]	233
	silicon _{liquid} [45]	2520
Melting temperatur e [K]	gold	1340
	silicon	1683
Thermal conductivit y [J s ⁻¹ m ⁻¹ K ⁻¹]	gold _{solid} [46]	$337 - 6.67 \cdot 10^{-2} T$
	gold _{liquid} [46]	152
	silicon _{solid} [47]	$25 + 422 e^{(-3.92 \cdot 10^{-3} T)}$
	silicon _{liquid} [48]	45.6
Specific heat capacity [J kg ⁻¹ K ⁻¹]	gold _{solid} [49]	$0.032 T + 118$
	gold _{liquid} [49]	152
	silicon _{solid} [45]	$4.2 \cdot 10^{-8} T^3 - 4.36 \cdot 10^{-5} T^2 + 3.90 T + 2.28 \cdot 10^4$
	silicon _{liquid} [45]	1100
Latent heat [J mol ⁻¹]	gold	12400
	silicon	36960

2.4.2 Integral geometry analysis

Integral geometry analyses such as the computation of Minkowski measures are elegant methods for studying the connectivity of different structures [28]. Minkowski measures are used to compare structures with each other and to identify related structures [19]. These structures can be of natural or simulated origin. In this study, the mathematical tool will be used to determine whether structures are of random or ordered origin, respectively induced or spinodal dewetting. A structure may be based on a complex ordering mechanism causing it to appear random to the human eye although it is not. Integral geometry analysis as it has been applied here can only predict that an ordering mechanism exists, but not which one. A complete integral geometry analysis can be eased by a simple, graphical evaluation of the different primary quantities such as the total area, the boundary length, and the Euler-Poincaré characteristic [24] and secondary quantities such as the number of closed areas and the formal radii [50]. For this study, the geometry of the gold film after laser conditioning will be compared with perfectly random or perfectly ordered models to determine geometric relationships. Fig. 4 shows a model where the ordered and random distributions of holes with a radius of 80 units in a plane of 5000×5000 square units are examined. The software package MATHLAB® of MathWorks Inc. was used to place points on a rectangular plane according to different rules. For the distribution shown in Fig. 4a, all points are set to the same coordinate so that they superimpose each other. Fig. 4b shows a distribution where all points are aligned and their distance maximized. Here, the points and the resulting circles, which are used to symbolise holes, must not touch each other under any circumstances. In Fig. 4c, the points are randomly distributed over the plane. After setting the points for all distributions, circles with defined radii were drawn around them. Radii of 10 to 150 units are considered here. The exact radii were used for distributions such as in Figs. 4a and 4b, while a sharp Poisson distribution was used for the circles in the distributions such as in Fig. 4c. Consequently, Figs. 4a and 4b stands for perfectly ordered distributions, while Fig. 4c represents perfectly (Poisson) random arrangements. Each circle is a mark for a hole in the plane or, in the case of random distribution, for a part of a network of holes. These perfect distributions are compared with SEM images of the experiments showing holes within the treated gold layers during phase 1 and phase 2 dewetting. In this way, a degree of similarity between the experimental data and the perfectly ordered or random distributions are to be shown. For this purpose, three geometric quantities are considered: radius of the holes; total area of the holes; and the total circumference of the holes respectively the total boundary lengths of the networks. The graphical analysis was performed with the software package Wayne Rasbands ImageJ version 1.52a.

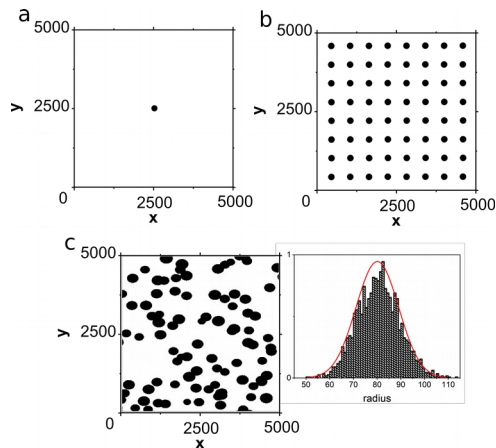


Figure 4. Calculated distribution of the holes. Two perfectly ordered distributions of holes with a radius of 80 units were calculated with MathWorks MATHLAB® on a 5000×5000 square unit plane (a,b). In a, all holes are superimposed, while in b, overlapping is strictly forbidden. (c) shows a perfectly ordered Poisson random distribution, where networks of holes may form. The inset shows the Poisson distribution for the radius of holes with an average value of 80 units.

3. Results

3.1 Generation of droplets

Silicon-gold samples were prepared as described and treated with a 266 nm nanosecond-laser, whereby the thin gold layer changes its shape and morphology. The resulting morphologies are strongly reminiscent of the different states of dewetting. Fig. 5 shows SEM images of gold layers after laser treatment (each after 100'000 pulses) in top view at different distances from the centre of the laser spot. The gold layer between the laser spots that is unaffected by the laser is shown in Figs. 5b and 5c. This corresponds to a completely untreated layer: a homogeneous gold layer without major disturbances or defects. At a distance of 35 μm to 50 μm from the centre of the laser spot a spatial warping in the layer thickness can be observed (Figs. 5c and 5d). A few isolated holes are also evident. This resembles the appearance of phase 1 of spinodal dewetting. In a similar way, the laser-induced gold nanostructure shown in Figs. 5g and 5h corresponds to phase 2. Warping can also be seen here. However, the valleys reach the silicon substrate, creating holes and networks of holes that lead to a net-like system of gold nanostructures. These networks exist at a distance of 15 μm to 35 μm from the centre of the laser spots. At smaller distances, the laser-induced structures turn into gold droplets with a size of a few hundred nanometres to a few micrometres (Figs. 5g and 5h). Fig. 5i shows the SEM image of a segment of a laser spot in top view. It can be seen here that the change in morphology has sharp edges (at approx. 15 μm and 35 μm). For 1'000 and 10'000 pulses same distances of morphology changes were found and thus not shown here separately. A substructure

reminiscent of plasmonic resonance effects can also be identified between the drops in fig. 5h and in phase 1 and phase 2 in fig. 5d and 5f. This laser-induced substructure consists of parallel lines with a distance of the laser wavelength (266 nm). Remarkably, these substructures are not visible in laser treated gold layers with an initial thickness of less than 5 nm but are more refined with growing gold layer thickness.

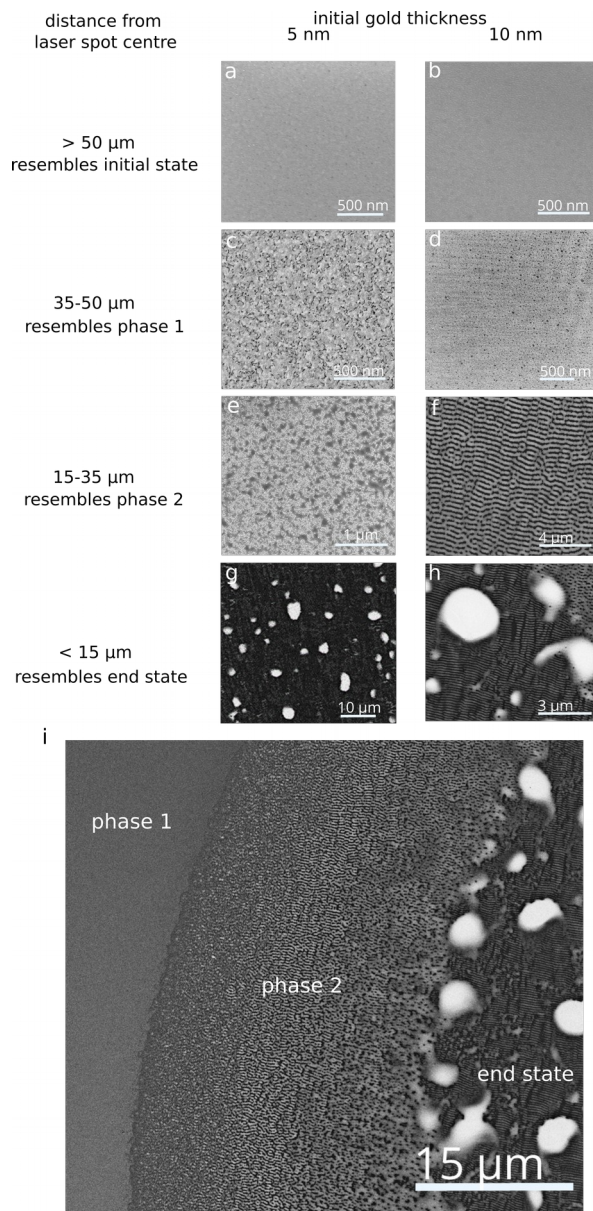


Figure 5. Dewetting phases after laser processing. All SEM top-view-images show gold layers respectively structures on (100)silicon wafers after laser conditioning of 100'000 pulses of a 266 nm nanosecond laser. (a), (c), (e), and (g) show the results for an initial gold layer thickness of 5 nm at different distances from the laser spot centre. Whereas (b), (d), (f), and (h) show results for an initial gold layer thickness of 10 nm. In the regions of the laser processed layers different dewetting states can be recognized. (i) shows the state boundary's in a segment of the laser spot. In its initial state, the gold layer is as grown. The SEM image shows grains. Phase 1 shows fluctuations in the gold layer and insulated holes. In the images of phase 2 the fluctuations reach the substrate. In the final state droplets can be seen.

Droplet size also change with initial gold thickness and number of pulses (Table 2). As the initial gold layer thickness increases, the droplets become larger. In general, the morphology alterations at greater thicknesses appear to occur only at higher pulse numbers. This means, the distances of the phase boundaries from the centre of the laser spot increase with higher number of pulses. At low thicknesses or high number of pulse, there are also areas near the centre where no gold, neither as a layer nor as drops, can be detected. With more than 100'000 pulses, no gold was detected in any sample in the entire laser spot, regardless of the initial gold thickness. Melting of silicon was never detected.

Table 2. Size of gold droplets. The size of gold droplets increases with rising thickness of the initial layer and with the number of laser pulses.

Size of gold droplets after laser treatment		Thickness of initial gold layer		
		1 nm	5 nm	10 nm
pulsesNumber of	1'000	50 nm	100 nm	\
	10'000	50 nm	500 nm	1500 nm
	100'000	60 nm	3000 nm	4000 nm

Fig. 6 shows SEM images of gold layers thermally treated by 800 K for 10 min. Different phases can be seen there, too. However, only one state, respectively one intermediate state, could be detected for each layer thickness. Drops of different sizes are formed at 1 nm (Fig. 6a). Structures similar to phase 2 and droplet like bodies are observable at 5 nm (Fig. 6b). Gold layers with a 10 nm thick gold layer (Fig. 6c) show early phase 2 and late phase 1 behaviour. In any case, the gold structures appear larger than in the laser-treated samples. At 1400 K samples of all considered gold thicknesses form droplets.

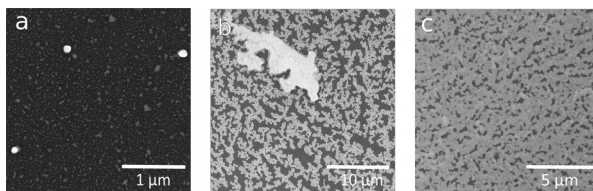


Figure 6. SEM images of gold layers after thermal treatment. Layers with different thickness of 1 nm (a), 5 nm (b), and 10 nm (c) were heated up to 800 K for 10 min. In dependence of the layer thickness different morphologies occur: (a) droplets, (b) late phase 2 morphology, and (c) early phase 2.

3.2 Modelling

3.2.1 COMSOL Multiphysics® simulation

Fig. 7 shows the results of the temperature simulations using the COMSOL Multiphysics® software package.

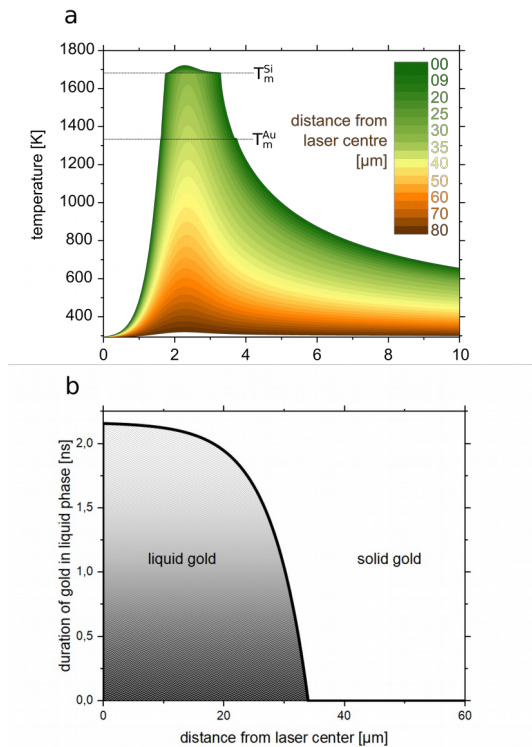


Figure 7. Results of simulations by COMSOL Multiphysics®. (a) shows the temperature of the gold layer at different times after the initiation of the laser pulse (x-axis) and at different distances to the laser spot centre (colour map). The platforms at 1337 K and 1687 K correspond to the melting points of gold and silicon. (b) shows a possible interpretation of the simulation: The duration, in which the gold stays liquid, in dependence of the distance from the laser spot centre.

Fig. 7a illustrates the calculated temperatures of a 5 nm gold layer in time and space for a 266 nm 190 μJ laser pulse. Since the laser pulse is described as a Gaussian function, the resulting temperature also resembles a bell-shaped distribution with a peak height of 1720 K at 2.4 ns in the centre of the laser spot. Afterwards, the temperature decreases according to heat equation, except at 1337 K and 1687 K. These are the melting points of gold and silicon, respectively, at which solidification heat is released into the system, causing unsteady behaviour. The colour map in Fig. 7a corresponds to the distance from the centre of the laser spot. According to this simulation, the silicon melts from the laser centre up to a distance of 30 μm from the centre of the laser spot. However, no melting was observed in the practical experiments. Fig. 7b simplifies the results of the simulation for the duration the gold remains liquid at different distances from the laser centre. According to this, liquid gold can be assumed at distances below 34 μm . At the centre, the gold remains liquid for the longest time per pulse with 2.2 ns.

3.2.2 Minkowski measures

Minkowski measures are used to compare structures with each other and to identify related structures. Fig. 8 shows this kind of Minkowski measures for the obtained data in a graphical version.

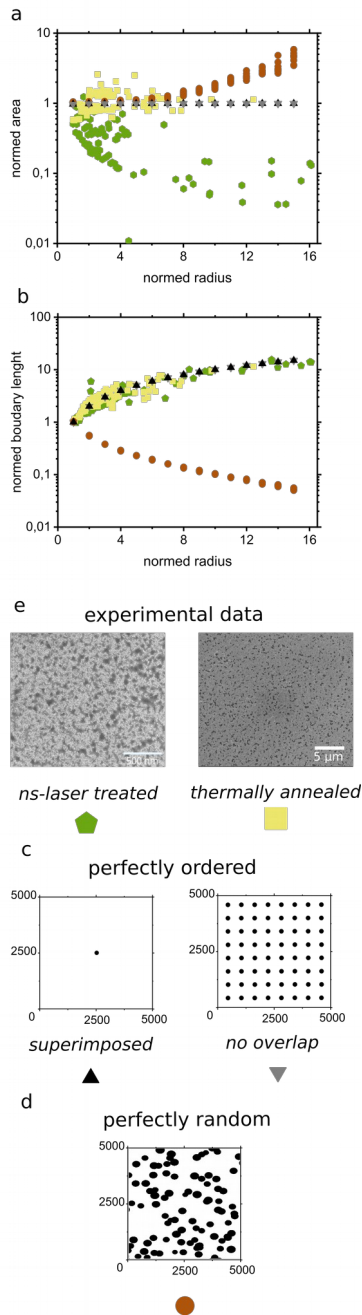


Figure 8. Minkowski measurement. In order to compare the experimental data with the perfect distribution models by Minkowski measures, a graphical analysis was performed by ImageJ. The graphs show the results of the measures with respect to the normalized area (d) and the boundary length (e) of the holes to their radii. The perfectly ordered values (black and grey triangles, a) overlap, while the perfectly (Poisson) random distribution (blue circles, b) behaves differently. The experimental data (red and green polyhedral, c) behave more like the ordered distributions.

Five different structures respectively networks of holes are compared: Two structures are perfectly ordered (Fig. 8a); one structure is perfectly random (Poisson distributed, Fig. 8b); and two are derived from experimental data (Fig. 8c). The experimental data come from the laser experiments and from the thermal processing of silicon-gold samples. In both cases, the connected holes in the phase 2 area and the few isolated holes in the phase 1 areas are considered. Figs. 8d and 8e shows the results of calculation of Minkowski measurement, where the behaviour of the hole area and the sum of the hole circumference, respectively boundary length, of the structures and networks are compared with respect to the hole radii. All values are normalized to the smallest detected radii. According to the theory, the two perfectly ordered structures superimpose each other, while the perfectly random values differ significantly from them. The experimental data, as can be seen, behave more like the ordered structures. The holes produced by the experiments seem to be very congruent with the theoretically ordered structures.

4. Discussion

The aim of the presented work is to compare gold structures created by laser interaction with structures formed by thermal treatment. In addition, the different states of dewetting and their intermediate states are to be shown in order to examine the transition from one state to the other in more detail. Fig. 5 shows that this goal has been achieved. The silicon substrates with 1 nm, 5 nm and 10 nm initial gold thickness show all four states of dewetting after the nanosecond laser treatment: initial state, phase 1, phase 2, and final state respectively droplet state. Only the 10 nm layer at 1'000 pulses does not reach the droplet state, but stays in phase 2 at the laser centre.

However, the reason for the significant change in morphology is not a direct interaction between the 266 nm laser and the gold. Instead, the heat is generated predominantly in the underlying silicon substrate. The simulations made with the COMSOL Multiphysics® software package in Fig. 7 show the temperature of the gold layer heated by the heating silicon. The simulation takes into account the various material parameters, the penetration depth of the laser into the silicon, and the Gaussian shape of the laser in time and space. This also explains the shape of the temperature-time curve in Fig. 7a, which also resembles a bell-shape in combination with heat equation. Since the colour map corresponds to the distance to the centre of the laser spot, it can be seen that gold should melt up to a distance of 34 μm from the centre and silicon up to a distance of 30 μm . However, the practical results do not support the hypothesis of molten silicon during the process. Even in the centre of the laser spot no evidence of a molten substrate can be found. Either the model overestimates the temperature here, or the melting process of the silicon is kinetically inhibited. One possibility is that

the heat is exchanged into the gold or silicon bulk faster than a melting process of the silicon surface can take place. Since gold cannot give off its heat to the bulk material, but can only cool down by heat radiation into the void, the simulation seems to fit much better here than for the silicon substrate. In contrast, the distance of 34 μm for liquid gold matches the practical results very closely, as the transition from the phase 1 to phase 2 lies at 35 μm . This indicates that only phase 2 and the final state occur as classical fluid dewetting, but phase 1 as solid state dewetting. To initiate a dewetting process, the material does not necessarily have to be liquid. In general, the state of aggregation is a macroscopic effect with limited significance on the nanometre scale. For dewetting it is especially important that the mobility of the particles, in this case the gold atoms, is high enough for the dewetting process. This can be done in a formal solid state - also known as solid state dewetting [1]. Fig. 7b shows how long the gold remains in liquid state at various distances from the laser centre. Since it is known from the simulations that the gold layer cools down completely between the pulses, it can be assumed that the effect of one pulse multiplied by 1'000 is the same as 1'000 consecutive pulses. The same applies, of course, to 10'000 and 100'000 pulses. In this context, it is obvious that it is not only how long the gold remains liquid that matters, but also how much energy is introduced during each heat-up. For example, a 10 nm gold layer at 10 μm from the centre after 10'000 pulses was liquid for $2.07 \times 10'000 = 20'700$ ns. According to the experimental data, the result is droplets of the final state. On the other hand, a 10 nm gold layer at 25 μm distance from the centre shows a phase 2 behaviour after 100'000 pulses, although it was in liquid state for much longer time, namely $1.66 \times 100'000 = 166'000$ ns. Accordingly, the local input energy is of higher relevance for the morphology formed than the time the gold layer remains liquid. One reason for this is the activation energy for each state. Values between 4.2 kJ mol^{-1} and 4.3 kJ mol^{-1} [51][52][53] can be found for the activation energy of the movement of gold atoms on silicon by various processes such as diffusion, nucleation, dewetting or Ostwald ripening. These different processes and the different stages indicate that droplet formation is not a single effect, but a correlation between a high number of effects and phenomena with different activation energies. While an energy of 230 kJ mol^{-1} at 10 μm (see equation 1) is sufficient to heat the system up and initiate a droplet structure, 200 kJ mol^{-1} at 25 μm is not sufficient, although the gold may remain liquid for longer at 25 μm than at 15 μm under certain circumstances. Table 3 shows the maximum energies required to activate the state transition calculated from the experimental data and the lateral decline of the laser energy.

Table 3. Activation energies of the state transitions. The experimental data reveal the distances of the phase transitions from the laser spot centre. At these local distances the activation energy for the phase transition has to be achieved. With support of equation 1 the maximal energy at these points can be calculated.

transition	Max. activation energy [kJ mol ⁻¹]
------------	---

initial state to phase 1 at 50 μm from centre	1.9
phase 1 to phase 2 at 35 μm from centre	2.4
phase 2 to final state at 15 μm from centre	4.2

Once a state is formed, the time the gold remains liquid comes into play more strongly: as soon as the activation energy is reached, the morphology changes and the structures grow. This is particularly evident in the size of the droplets in the final state (Figs. 5g and 5h). Table 2 shows here the dependence of droplet size on the layer thickness h and the number of pulses n .

Empirical data in the literature show a dependence of $h^{5/3}$ for droplet size in thermally treated layers. As an approximation it can be assumed that the droplet size for short ranges increases linearly with the number of pulses. Fig. 9 shows that these correlations apply not only to thermally treated gold layers but also to nanosecond laser treated layers. Consequently, the mechanism of dewetting in the thermal process and in laser conditioning is not only theoretically the same, but also leads to the same empirical observations.

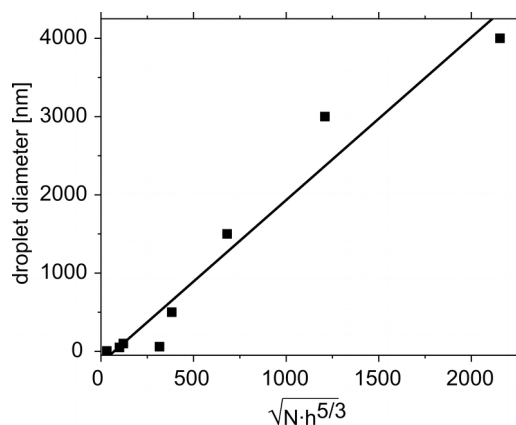


Figure 9. Correlation between droplet size, number of pulses (N) and initial height of the gold layer (h) for droplets generated by nanosecond laser conditioning.

The major advantage of laser treatment is its better controllability. With finely adjustable input energies, laser profiles in time and space and the number of pulses, many more parameters can be controlled than with thermal treatment. Thus the structures can be controlled in more detail and better adapted to specific applications. If, for example, the gold droplets are used as a catalyst for the growth of nanowires, the diameter of the nanowire depends strongly on the droplet size, which can be adjusted more easily with a laser treatment than with thermal exposure. Moreover, the synthesis

of all dewetting states on one single substrate was only possible by the laser-matter interaction carried out here and not by thermal treatment. Nevertheless, it must be mentioned that the laser interaction creates at least one additional substructure. Due to the high plasmonic resonance of the gold, a substructure is formed which generates parallel lines with a distance of the laser wavelength (266 nm). It is known that gold on silicon forms a thin wetting layer consisting of only a few monolayers. Presumably, the plasmonic resonance can build up an oscillation within the wetting layer and thus form the observed substructure. The existence of a wetting layer of gold on silicon has already been proven elsewhere in the literature [52][54]. The results there also indicate the option of an energy-induced subsequent deformation of the wetting layer. In this study, such a warping seems to occur due to the oscillation of the free electron gas density.

The thermally treated samples form nothing but droplets when heated above the melting temperature of gold. Nevertheless, the morphologies of phase 1 and phase 2 could be isolated at much lower temperatures. Here all states occur by solid state dewetting, in which the material may be formally solid and not liquid. This is particularly true for gold on silicon because of the high chemical affinity between silicon and gold: at temperatures above 550 K, silicon can dissolve inside the gold and vice versa [55]. In this way, the system is able to form alloys or even eutectics locally, which increases local mobility many times over. Fortunately, the increase in mobility is not high enough to form droplets immediately in all cases, but only to isolate phase 1 morphologies in 10 nm gold samples and phase 2 morphologies in 5 nm samples.

The Minkowski measures in Fig. 8 show that there is no significant difference between laser-induced and thermally induced structures. It is clearly shown that perfectly ordered systems behave differently in respect to the Minkowski measures than perfectly random systems. This is also true for systems where it is not possible to recognize an order or a randomness with the eyes. By the measures the graphs show that both laser- and thermally treated morphologies behave rather like well-ordered systems. This is particularly evident with regard to the boundary length (Fig. 8e). Only the experimental data of the laser experiment for the normalized area in Fig. 8d do not exactly match the perfectly ordered systems. However, it behaves even less than the perfectly (Poisson) random system. This can happen when several opposing phenomena occur simultaneously. The tendency towards the well-ordered systems shows that spinodal dewetting is the main process here. Yet other processes also take place - especially in the case of laser-treated samples. Induced dewetting occurs spontaneously or after mechanical action. A later process therefore increases the possibility for these occasions. Additionally, plasmonic resonance takes place. The Minkowski measures cannot say which additional effects are involved, but they show that it is obvious that the structures formed by laser

and thermally treated have an internal order. This order is probably formed from an internal, self-amplified oscillation, as it only occurs of a spinodal dewetting.

5. Conclusion

Most important aspects for an industrial process are reliability and versatility. To be recognised, a scientific method must be reproducible. In this study, a laser treatment process proved to be more controllable than the classical thermal treatment in selective dewetting processes aimed at forming nanoparticles such as nanodroplets, since the laser process includes more adjustable parameters such as pulse energy, number of pulses and pulse duration. Gold droplets are created by the interaction of a 266 nm nanosecond laser with a thin gold layer on silicon. These droplets show a very similar behaviour to the thermally treated droplets. In fact, both processes are induced by heat introduced into the gold layer. Since the laser energy is predominantly absorbed inside the silicon, the gold layer heats up indirectly. With the laser process it is possible to warm the gold very selectively. In this way, not only droplets are obtained, but also the different states of dewetting, such as the morphologies of phase 1 and phase 2. To our knowledge, it has never been possible to separate each dewetting state on a single thermally treated sample. Due to the high adjustability of the laser, this was possible here with laser-treated samples. This allows a more in-depth clarification of the dewetting mechanisms and the transition between the states. Here it is shown that there is no smooth transition between the states, but sharp boundaries. Taking temperature simulations with the software package COMSOL Multiphysics® into account, it has been shown that the duration of how long the gold remains liquid is not the critical parameter for determining which state is formed. Rather, it is the energy applied that is crucial: the transitions appear to have separate activation energies quantified here. The duration of how long the gold remains liquid only influences how intense the state is formed, e.g. how large the droplets grow.

Minkowski measures were used to determine which of the both following mechanisms effectively happens: induced dewetting, which occurs randomly or by mechanical impact, or spinodal dewetting, which occurs by internal self-amplified material warping. The holes in the gold layer, which form during phase 1 and phase 2 as the primary state of the droplets, were taken into account. The holes in the experimental samples, laser treated and thermally treated, were compared with perfectly ordered and perfectly (Poisson) random models. It was found that both types of experimental structures show more similarities with the ordered models. This clearly indicates that spinodal dewetting is the main process. Nevertheless, other secondary phenomena also come into play. For example, substructures are visible on the laser-treated samples. These structures appear as lines

with a distance of the laser wavelength and are most likely formed as a result of the plasmonic resonance of the wetting layer between the droplets with the laser.

In summary, it was shown that the high adjustability of the interaction between a nanosecond laser and a thin metal layer can be exploited to gain a deeper insight into the mechanisms of dewetting and the energetic requirements needed for the different states of dewetting. Since the morphology of the system and the size and shape of the resulting droplets can be controlled in great detail, this laser interaction is very promising for further research with high reproducibility needs and for industrial processes requiring reliability and versatility. An example of both is the growth of silicon nanowires, whose diameter and length are crucial for their application. Since gold droplets are used as catalysts for nanowire growth and their size and shape determine the properties of the nanowires, laser-induced dewetting can help to bring silicon nanowire technology to a new, more industrial standard.

7. Declaration of interests

The authors declare that they have no known competing financial interests or personal relationships that could have appeared to influence the work reported in this paper.

References

- [1] C. V Thompson, Solid-state dewetting of thin films, *Annu. Rev. Mater. Res.* 42 (2012) 399–434.
- [2] P.G. de Gennes, Wetting: statics and dynamics, *Rev. Mod. Phys.* 57 (1985) 827–863. <https://doi.org/10.1103/RevModPhys.57.827>.
- [3] R. Seemann, S. Herminghaus, K. Jacobs, Dewetting Patterns and Molecular Forces: A Reconciliation, *Phys. Rev. Lett.* 86 (2001) 5534–5537. <https://doi.org/10.1103/PhysRevLett.86.5534>.
- [4] NobelPrize.org, The Nobel Prize in Physics 1991, (n.d.).
- [5] P.-G. de Gennes, Soft Matter (Nobel Lecture), *Angew. Chemie Int. Ed. English.* 31 (1992) 842–845. <https://doi.org/10.1002/anie.199208421>.
- [6] I. Langmuir, Oil Lenses on Water and the Nature of Monomolecular Expanded Films, *J. Chem. Phys.* 1 (1933) 756–776. <https://doi.org/10.1063/1.1749243>.
- [7] R. Seemann, S. Herminghaus, K. Jacobs, Gaining control of pattern formation of dewetting liquid films, *J. Phys. Condens. Matter.* 13 (2001) 4925–4938. <https://doi.org/10.1088/0953-8984/13/21/319>.
- [8] R. Seemann, S. Herminghaus, K. Jacobs, Shape of a Liquid Front upon Dewetting, *Phys. Rev. Lett.* 87 (2001) 196101. <https://doi.org/10.1103/PhysRevLett.87.196101>.
- [9] H. Krishna, C. Favazza, A.K. Gangopadhyay, R. Kalyanaraman, Functional nanostructures through nanosecond laser dewetting of thin metal films, *Jom.* 60 (2008) 37–42.
- [10] F. Ruffino, A. Pugliara, E. Carria, C. Bongiorno, C. Spinella, M.G. Grimaldi, Formation of

- nanoparticles from laser irradiated Au thin film on SiO₂/Si: Elucidating the Rayleigh-instability role, *Mater. Lett.* 84 (2012) 27–30.
- [11] F. Ruffino, A. Pugliara, E. Carria, L. Romano, C. Bongiorno, G. Fiscaro, A. La Magna, C. Spinella, M.G. Grimaldi, Towards a laser fluence dependent nanostructuring of thin Au films on Si by nanosecond laser irradiation, *Appl. Surf. Sci.* 258 (2012) 9128–9137.
- [12] D. Wang, P. Schaaf, Thermal dewetting of thin Au films deposited onto line-patterned substrates, *J. Mater. Sci.* 47 (2012) 1605–1608. <https://doi.org/10.1007/s10853-011-5716-0>.
- [13] S. Yadavali, M. Khenner, R. Kalyanaraman, Pulsed laser dewetting of Au films: Experiments and modeling of nanoscale behavior, *J. Mater. Res.* 28 (2013).
- [14] C. Favazza, R. Kalyanaraman, R. Sureshkumar, Robust nanopatterning by laser-induced dewetting of metal nanofilms, *Nanotechnology.* 17 (2006) 4229.
- [15] H.A. El-Sayed, C.A. Horwood, E. Owusu-Ansah, Y.J. Shi, V.I. Birss, Gold nanoparticle array formation on dimpled Ta templates using pulsed laser-induced thin film dewetting, *Phys. Chem. Chem. Phys.* 17 (2015) 11062–11069.
- [16] C. Ehlers, S. Kayser, D. Uebel, R. Bansen, T. Markurt, T. Teubner, K. Hinrichs, O. Ernst, T. Boeck, In situ removal of a native oxide layer from an amorphous silicon surface with a UV laser for subsequent layer growth, *CrystEngComm.* 20 (2018) 7170–7177. <https://doi.org/10.1039/C8CE01170B>.
- [17] COMSOL Inc, (2017).
- [18] J. Trice, D. Thomas, C. Favazza, R. Sureshkumar, R. Kalyanaraman, Pulsed-laser-induced dewetting in nanoscopic metal films: Theory and experiments, *Phys. Rev. B.* 75 (2007) 235439. <https://doi.org/10.1103/PhysRevB.75.235439>.
- [19] K.R. Mecke, Integral Geometry in Statistical Physics, *Int. J. Mod. Phys. B.* 12 (1998) 861–899. <https://doi.org/10.1142/S0217979298000491>.
- [20] D. Legland, K. Kiêu, M.-F. Devaux, COMPUTATION OF MINKOWSKI MEASURES ON 2D AND 3D BINARY IMAGES, *Image Anal. Stereol. Vol 26, No 2.* (2011). <https://doi.org/10.5566/ias.v26.p83-92>.
- [21] M. Einasto, L.J. Liivamägi, E. Tempel, E. Saar, E. Tago, P. Einasto, I. Enkvist, J. Einasto, V.J. Martínez, P. Heinämäki, P. Nurmi, The sloan great wall. morphology and galaxy content, *Astrophys. J.* 736 (2011) 51. <https://doi.org/10.1088/0004-637X/736/1/51>.
- [22] M. Biernacka, P. Flin, Dynamic evolution of nearby galaxy clusters, *Astron. Nachrichten.* 332 (2011) 537–544. <https://doi.org/10.1002/asna.200911554>.
- [23] A. Wiegand, T. Buchert, M. Ostermann, Direct Minkowski Functional analysis of large redshift surveys: a new high-speed code tested on the luminous red galaxy Sloan Digital Sky Survey-DR7 catalogue, *Mon. Not. R. Astron. Soc.* 443 (2014) 241–259. <https://doi.org/10.1093/mnras/stu1118>.
- [24] K.R. Mecke, Morphological characterization of patterns in reaction-diffusion systems, *Phys. Rev. E.* 53 (1996) 4794–4800. <https://doi.org/10.1103/PhysRevE.53.4794>.
- [25] G.J.A. Sevink, A. V. Zvelindovsky, Kinetic pathways of sheared block copolymer systems derived from Minkowski functionals, *J. Chem. Phys.* 121 (2004) 3864–3873. <https://doi.org/10.1063/1.1774982>.
- [26] A. Grayeli Korpi, Ş. Tǎlu, M. Bramowicz, A. Arman, S. Kulesza, B. Psczolkowski, S. Jurečka, M.

- Mardani, C. Luna, P. Balashabadi, S. Rezaee, S. Gopikishan, Minkowski functional characterization and fractal analysis of surfaces of titanium nitride films, *Mater. Res. Express.* 6 (2019) 086463. <https://doi.org/10.1088/2053-1591/ab26be>.
- [27] K. Jacobs, S. Herminghaus, K.R. Mecke, Thin Liquid Polymer Films Rupture via Defects, *Langmuir.* 14 (1998) 965–969. <https://doi.org/10.1021/la970954b>.
- [28] S. Herminghaus, K. Jacobs, K. Mecke, J. Bischof, A. Fery, M. Ibn-Elhaj, S. Schlagowski, Spinodal Dewetting in Liquid Crystal and Liquid Metal Films, *Science* (80-.). 282 (1998) 916 LP – 919. <https://doi.org/10.1126/science.282.5390.916>.
- [29] K.J. Berean, V. Sivan, I. Khodasevych, A. Boes, E. Della Gaspera, M.R. Field, K. Kalantar-Zadeh, A. Mitchell, G. Rosengarten, Laser-Induced Dewetting for Precise Local Generation of Au Nanostructures for Tunable Solar Absorption, *Adv. Opt. Mater.* 4 (2016) 1247–1254.
- [30] Y. Oh, J. Lee, M. Lee, Fabrication of Ag-Au bimetallic nanoparticles by laser-induced dewetting of bilayer films, *Appl. Surf. Sci.* 434 (2018) 1293–1299.
- [31] L. Yu, B. O'Donnell, P.-J. Alet, S. Conesa-Boj, F. Peiró, J. Arbiol, P.R. i Cabarrocas, Plasma-enhanced low temperature growth of silicon nanowires and hierarchical structures by using tin and indium catalysts, *Nanotechnology.* 20 (2009) 225604. <https://doi.org/10.1088/0957-4484/20/22/225604>.
- [32] F. Lange, O. Ernst, T. Teubner, C. Richter, M. Schmidbauer, O. Skibitzki, T. Schroeder, P. Schmidt, T. Boeck, In-plane growth of germanium nanowires on nanostructured Si(001)/SiO₂ substrates, *Nano Futur.* (2020). <https://doi.org/10.1088/2399-1984/ab82a0>.
- [33] A.I. Boukai, Y. Bunimovich, J. Tahir-Kheli, J.-K. Yu, W.A. Goddard, J.R. Heath, Silicon nanowires as efficient thermoelectric materials, in: *Mater. Sustain. Energy*, Co-Published with Macmillan Publishers Ltd, UK, 2010: pp. 116–119. https://doi.org/10.1142/9789814317665_0018.
- [34] M.Y. Swinkels, I. Zardo, Nanowires for heat conversion, *J. Phys. D. Appl. Phys.* 51 (2018) 353001. <https://doi.org/10.1088/1361-6463/aad25f>.
- [35] G. Gadea, M. Pacios, Á. Morata, A. Tarancón, Silicon-based nanostructures for integrated thermoelectric generators, *J. Phys. D. Appl. Phys.* 51 (2018) 423001. <https://doi.org/10.1088/1361-6463/aad683>.
- [36] L. Filipovic, T. Grasser, Editorial for the Special Issue on Miniaturized Transistors, *Micromachines.* 10 (2019). <https://doi.org/10.3390/mi10050300>.
- [37] G. Hu, H. Edwards, M. Lee, Silicon integrated circuit thermoelectric generators with a high specific power generation capacity, *Nat. Electron.* 2 (2019) 300–306. <https://doi.org/10.1038/s41928-019-0271-9>.
- [38] Y.Y. Wu, M. Eizenberg, Effects of thermal treatment on structures of Cu/atomic-layer-deposited TaN films/Si stacks, *Thin Solid Films.* 514 (2006) 33–44. <https://doi.org/10.1016/J.TSF.2006.02.014>.
- [39] S. Kondati Natarajan, C.-L. Nies, M. Nolan, Ru passivated and Ru doped ϵ -TaN surfaces as a combined barrier and liner material for copper interconnects: a first principles study, *J. Mater. Chem. C.* 7 (2019) 7959–7973. <https://doi.org/10.1039/C8TC06118A>.
- [40] K. Takayanagi, Y. Kondo, H. Ohnishi, Suspended gold nanowires: ballistic transport of electrons, *JSAP Int.* 3 (2001).
- [41] T. Ogitsu, Y. Ping, A. Correa, B. Cho, P. Heimann, E. Schwegler, J. Cao, G.W. Collins, Ballistic

- electron transport in non-equilibrium warm dense gold, *High Energy Density Phys.* 8 (2012) 303–306.
- [42] H.D. Hallen, A. Fernandez, T. Huang, R.A. Buhrman, J. Silcox, Gold–silicon interface modification studies, *J. Vac. Sci. Technol. B Microelectron. Nanom. Struct. Process. Meas. Phenom.* 9 (1991) 585–589.
- [43] W.H. Haynes, *CRC Handbook of Chemistry and Physics*, 92nd ed., CRC Press, Boca Raton, 2011.
- [44] P.F. Paradisa, T. Ishikawaa, N. Koikeb, Density of liquid gold measured by a non-contact technique, *Gold Bull.* 41 (2008) 242–245. <https://doi.org/10.1007/BF03214876>.
- [45] L. Calcagnile, Laser induced phase transitions in Si and Ge implanted Si substrates, *Phys. Status Solidi.* 151 (1995) 23–32.
- [46] R.W. Powell, C.Y. Ho, P.E. Liley, *Thermal conductivity of selected materials*, US Department of Commerce, National Bureau of Standards Washington, DC, 1966.
- [47] M.C. Wingert, J. Zheng, S. Kwon, R. Chen, Thermal transport in amorphous materials: a review, *Semicond. Sci. Technol.* 31 (2016) 113003.
- [48] H. Nagai, Y. Nakata, T. Tsurue, H. Minagawa, K. Kamada, S.E. Gustafsson, T. Okutani, Thermal conductivity measurement of molten silicon by a hot-disk method in short-duration microgravity environments, *Jpn. J. Appl. Phys.* 39 (2000) 1405.
- [49] Y. Takahashi, H. Akiyama, Heat capacity of gold from 80 to 1000 K, *Thermochim. Acta.* 109 (1986) 105–109.
- [50] J. Becker, G. Grün, R. Seemann, H. Mantz, K. Jacobs, K.R. Mecke, R. Blossey, Complex dewetting scenarios captured by thin-film models, *Nat. Mater.* 2 (2003) 59–63. <https://doi.org/10.1038/nmat788>.
- [51] F. Leroy, Ł. Borowik, F. Cheynis, Y. Almadori, S. Curiotto, M. Trautmann, J.C. Barbé, P. Müller, How to control solid state dewetting: A short review, *Surf. Sci. Rep.* 71 (2016) 391–409. <https://doi.org/10.1016/J.SURFREP.2016.03.002>.
- [52] O.C. Ernst, F. Lange, D. Uebel, T. Teubner, T. Boeck, Analysis of catalyst surface wetting: the early stage of epitaxial germanium nanowire growth, *Beilstein Arch.* 2020 (2020) 75.
- [53] S. Curiotto, F. Cheynis, F. Leroy, P. Müller, Surface diffusion of Au on 3×3 Si(111)–Au studied by nucleation-rate and Ostwald-ripening analysis, *Surf. Sci.* 647 (2016) 8–11. <https://doi.org/https://doi.org/10.1016/j.susc.2015.11.015>.
- [54] J.B. Hannon, S. Kodambaka, F.M. Ross, R.M. Tromp, The influence of the surface migration of gold on the growth of silicon nanowires, *Nature.* 440 (2006) 69–71. <https://doi.org/10.1038/nature04574>.
- [55] N.A. Stolwijk, B. Schuster, J. Hölzl, H. Mehrer, W. Frank, Diffusion and solubility of gold in silicon, *Phys. B+ C.* 116 (1983) 335–342.